Topological Mott insulator with bosonic edge modes in one-dimensional fermionic superlattices

Haiping Hu ⬤,[1] Shu Chen,[2,3] Tian-Sheng Zeng,[1] and Chuanwei Zhang[1,*]

[1]*Department of Physics, The University of Texas at Dallas, Richardson, Texas 75080, USA*
[2]*Beijing National Laboratory for Condensed Matter Physics, Institute of Physics, Chinese Academy of Sciences, Beijing 100190, China*
[3]*School of Physical Sciences, University of Chinese Academy of Sciences, Beijing 100049, China*

We investigate topological phase transitions driven by interaction and identify a topological Mott insulator state in one-dimensional fermionic optical superlattices through a numerical density-matrix renormalization-group method. Remarkably, the low-energy edge excitations change from spin-1/2 *fermionic* single-particle modes to spin-1 *bosonic* collective modes across the phase transition. Due to spin-charge separation, the low-energy theory is governed by an effective spin superexchange model, whereas the charge degree of freedom is fully gapped out. Such topological Mott state can be characterized by a spin Chern number and gapless magnon modes protected by a finite spin gap. The proposed experimental setup is simple and may pave the way for the experimental observation of exotic topological Mott states.

I. INTRODUCTION

The interplay between single-particle band topology and many-body interaction plays a crucial role in many important strongly correlated phenomena in condensed-matter physics. Unlike single-particle topological states [1,2], interactions can induce remarkable physical phenomena such as fractionalization of emergent collective excitations and give rise to intriguing correlated states that exhibit nontrivial topological properties. Prominent examples are fractional quantum Hall effects [3,4], where constituent particles are electrons but emergent quasiparticles only carry fractions of electron charge, and topological Mott insulator [5] with deconfined spinon excitations.

One-dimensional (1D) interacting systems, which are amenable to exact methods, provide fundamental insights for understanding strongly correlated states. Due to the confined geometry, the low-energy excitations are collective and exhibit a peculiar fractionalization, spin-charge separation (SCS). A single-particle excitation is divided into two collective modes, which possess charge and spin degrees of freedom, respectively. In a topological Mott insulator, low-energy excitations lie in the spin sector, whereas charge excitations are frozen by strong interactions. The topological properties manifest themselves by the appearance of gapless modes at the boundary protected by the insulating bulk. In previous studies, these edge modes are composed of spinons [6,7] carrying spin-1/2 and no charge. As spinful modes can also carry integer spin (like magnon, spin-1), two natural and important questions need to be addressed. (i) Are there topological Mott insulator states hosting other types of spinful edge modes and how does one characterize them? (ii) Since SCS severely changes the low-energy excitations, what is the bulk-edge correspondence in a topological Mott insulator state?

In this paper, we address these two important questions by studying the Mott insulator states in a 1D fermionic optical superlattice. Ultracold atoms in optical lattices have provided unprecedented controllability to simulate strongly interacting systems. In particular, 1D optical superlattices open a simple avenue towards realizing exotic topological states [8–16] because of their exact correspondence with quantum Hall physics [17,18] in an extended space. Here we scrutinize Mott transitions in 1D optical superlattices and identify a topological Mott insulator using the quasiexact numerical density-matrix renormalization group (DMRG). Such Mott phase transition from a band topological insulator to a topological Mott insulator is accompanied by bulk excitation gap closing, SCS, and the change of spin Chern number. The corresponding low-energy excitations change from single-particle spin-1/2 fermionic modes to collective spin-1 bosonic modes, consistent with the spin Chern number change across the transition (i.e., bulk-edge correspondence). The low-energy physics is governed by an antiferromagnetic spin superexchange model due to SCS. Our proposed experimental setup involves fermions in a 1D triple-well superlattice and is simple to realize in experiments comparing to other complex lattice models or materials [5–7].

The remainder of this paper is organized as follows. In Sec. II, we introduce the Fermi-Hubbard model with a superlattice potential and show its topological properties on the single-particle level. In Sec. III, we demonstrate the topological Mott transition, accompanied by SCS with increasing interaction strength. Section IV is devoted to the bulk-edge correspondence. We show the emergence of different types of edge states and/or excitations before and after SCS. In Sec. V, we discuss the nontrivial (bosonic) magnon excitations in the topological Mott insulator. And finally, in Sec. VI, we draw conclusions and discuss the observations of the discovered topological Mott physics in current cold atom experiments. More technical details and numerical results are provided in the Appendix. In Appendix A 1, the 1D effective

---

*chuanwei.zhang@utdallas.edu

spin superexchange model is derived. Appendix A 2 further demonstrates the adiabatic continuity and topological properties of the spin superexchange model. In Appendix A 3, the entanglement spectrum is calculated as an identification of the Mott transition. Appendix A 4 presents the spatial charge and spin distributions for the many-body system. Appendix A 5 discusses the disorder effect.

II. SINGLE-PARTICLE PHYSICS

We consider 1D Fermi gases with two internal states (labeled by $\sigma = \uparrow, \downarrow$) tightly confined in transverse directions [Fig. 1(a)]. Two counterpropagating laser beams (wavelength λ) form a main optical lattice $V_0(x) = V_0 \cos^2(k_0 x)$ with $k_0 = 2\pi/\lambda$. Two additional laser beams (wavelength λ') incident at a tilt angle θ_0 form a secondary weak lattice $V_2(x) = V_2 \cos^2(k_2 x + \varphi)$ with $k_2 = 2\pi \cos \theta_0/\lambda'$ and relative phase φ with respect to the main lattice. As illustrated in Fig. 1(b), the total potential $V(x) = V_0(x) + V_2(x)$ forms a superlattice, with its period determined by the ratio $q = k_0/k_2 = \frac{\lambda'}{\lambda \cos \theta_0}$. Such an optical superlattice has been experimentally realized by many groups [19–21].

When the potential depth V_0 is much larger than the recoil energy $E_r = \hbar^2 k_0^2/2M$ (M is the atomic mass), only the lowest Bloch band needs to be considered and the system can be well approximated [22–25] by the following tight-binding model with a superlattice potential

$$H = \sum_{j=1,\sigma}^{L} [-t(c_{j\sigma}^{\dagger} c_{j+1\sigma} + \text{H.c.}) + \mu_j n_{j\sigma}] + U n_{j\uparrow} n_{j\downarrow}, \quad (1)$$

where $c_{j\sigma}$ annihilates a spin-σ fermion at jth site, L is the length of the chain, and $\mu_j = \mu \cos(2\pi j/q + \varphi)$ is the on-site (long period) superlattice potential. t is the hopping strength between nearest sites and hereafter set as the energy unit,

$t = 1$. A cyclical variation of φ brings back the Hamiltonian $H(\varphi) = H(\varphi + 2\pi)$, which is crucial for topological Thouless pumping [26] and the evolution of edge modes. The superlattice phase φ provides a synthetic dimension to mimic 2D topological physics [8–16]. The interaction U between atoms can be tuned over a wide range via Feshbach resonance or confinement induced resonance [27] for 1D systems. At half-filling, the Hamiltonian remains invariant under the simultaneous transformations $\varphi \to \varphi + \pi$ and $c_{j\sigma} \to c_{j\bar{\sigma}}^{\dagger}$, yielding an energy spectrum of period π on φ.

In this paper, we elaborate on the $q = 3$ case and the generalization to other periods is straightforward. For the incommensurate case, the interaction can induce many-body localization [21]. Since each unit cell has three sites, the single-particle spectrum contains three bands [Fig. 1(c)]. Different from a normal insulator, there are end modes connecting adjacent bands in each gap under open boundary condition (OBC). Under periodic boundary condition (PBC), these end modes merge into bulk bands and disappear. The nontrivial band topology is characterized by Chern number [8–14]

$$\mathcal{C} = \frac{1}{2\pi} \iint d\theta \, d\varphi \, F(\theta, \varphi), \quad (2)$$

formulated in the 2D parameter space spanned by $(\theta, \varphi) \in [0, 2\pi] \times [0, 2\pi]$, where θ is introduced by imposing a twist boundary condition [28,29] $\Psi_{j+L} = \Psi_j e^{i\theta}$ on the wave function, and $F(\theta, \varphi) = \text{Im}(\langle \frac{\partial \Psi}{\partial \varphi} | \frac{\partial \Psi}{\partial \theta} \rangle - \langle \frac{\partial \Psi}{\partial \theta} | \frac{\partial \Psi}{\partial \varphi} \rangle)$ is the Berry curvature. $\mathcal{C} = 1$ and -1 when the chemical potential lies in the first and second band gaps, respectively. According to bulk-edge correspondence, the Chern number is equal to the number of chiral edge states by adiabatically evolving φ, as long as the bulk gap remains finite in the whole process [26,30–32].

III. TOPOLOGICAL MOTT TRANSITION AND SPIN-CHARGE SEPARATION

Now we consider an interacting many-body system $(N_\uparrow, N_\downarrow)$ composed of $N_\uparrow$ spin-up and $N_\downarrow$ spin-down atoms on the above superlattice. Both total density $\rho = \sum_{j,\sigma} n_{j\sigma}/L$ and magnetization $m = \sum_j (n_{j\uparrow} - n_{j\downarrow})/L$ are conserved quantities. We denote the nth lowest eigenenergy and corresponding wave function as $E_n(N_\uparrow, N_\downarrow)$ and $\Psi_n(N_\uparrow, N_\downarrow)$, respectively. $n = 0$ then refers to the many-body ground state. In the subsequent DMRG calculations, density-matrix eigenstates are kept dynamically to ensure the discarded weight less than 10^{-9}. The maximum truncation error of the ground-state energy is about 10^{-7} and in general 10–15 sweeps are enough to reach the required precision.

We utilize three different bulk excitation gaps to characterize the low-energy modes: charge gap $\Delta_c = [E_0(N_\uparrow + 1, N_\downarrow + 1) + E_0(N_\uparrow - 1, N_\downarrow - 1) - 2E_0(N_\uparrow, N_\downarrow)]/2$ with a fixed magnetization m, spin gap $\Delta_s = [E_0(N_\uparrow + 1, N_\downarrow - 1) + E_0(N_\uparrow - 1, N_\downarrow + 1) - 2E_0(N_\uparrow, N_\downarrow)]/2$ with a fixed density ρ, and neutral gap $\Delta_{ne} = E_1(N_\uparrow, N_\downarrow) - E_0(N_\uparrow, N_\downarrow)$. The neutral gap directly gives the lowest excitation energy of the many-body system $(N_\uparrow, N_\downarrow)$.

We concentrate on the half-filling case with $\rho = 1$ and $m = -1/3$. In the noninteracting limit, the two-component fermionic atoms populate single-particle levels from low to
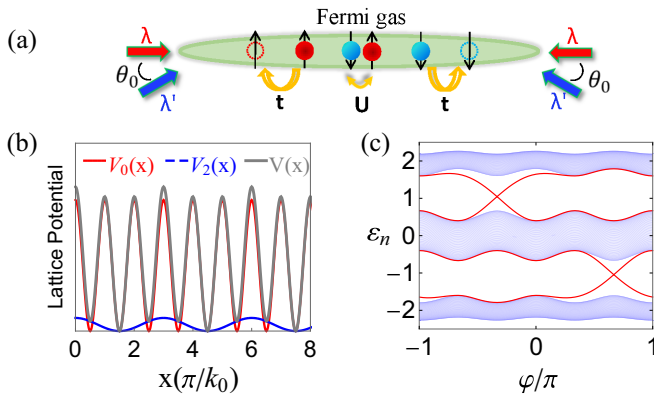

FIG. 1. (a) Schematics of experimental setup. A two-component Fermi gas is tightly confined in 1D. Two counterpropagating lasers (wavelength λ) form the main lattice, while two lasers (wavelength λ') incident at an angle θ_0 form the secondary weak long-period lattice. t and U denote the hopping and interspecies interaction strength, respectively. (b) The resulting lattice potentials. The local minima of the total potential $V(x)$ are located at the minima of the main lattice. (c) Single-particle bands with respect to superlattice phase φ under OBC. Red lines highlight the end modes. $q = 3$, $\mu = 1.2$, and $L = 240$.

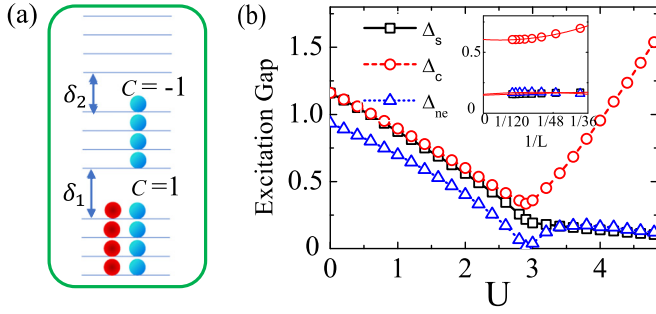FIG. 2. (a) Sketch of level occupation in noninteracting limit with $\rho = 1$ and $m = -1/3$. δ_1 and δ_2 denote the single-particle band gaps, characterized by $\mathcal{C} = \pm 1$, respectively. (b) The spin gap Δ_s (black square), charge gap Δ_c (red circle), and neutral gap Δ_{ne} (blue triangle) as a function of interaction U with $L = 72$ lattice sites. The inset shows finite-size analysis of the three gaps at $U = 3.5$. The red lines are from polynomial fitting. $\varphi = 0$; $\mu = 1.2$.

high independently as sketched in Fig. 2(a). The spin-up atoms are filled up to the first band gap (denoted as δ_1) and spin-down atoms to the second band gap (denoted as δ_2). Because two band gaps are characterized by opposite Chern numbers $\mathcal{C} = \pm 1$, the system is in a quantum spin Hall–like state with a spin Chern number $\mathcal{C}_s = 2$ [33,34], which is defined by Eq. (2) through choosing $\theta_\uparrow = -\theta_\downarrow$ for the twisted boundary condition. Here a single-particle excitation should overcome the band gaps and carry both charge and spin degree of freedom. The spin and charge gaps are equal, determined by $\Delta_s = \Delta_c = (\delta_1 + \delta_2)/2$ because spin and charge modes are tightly bound together. $\Delta_{ne} = \min\{\delta_1, \delta_2\}$ in this case.

With increasing interaction, the spin and charge modes would exhibit totally different behaviors. Figure 2(b) plots the three gaps with respect to U. Due to the repulsion between different components, the atoms prefer occupying higher levels. Starting from the same value, both Δ_c and Δ_s decrease first. Δ_c arrives at its minimum at $U_c \approx 2.9$, where Δ_{ne} closes. Δ_c and Δ_s coincide with each other at $U < U_c$, revealing that spin and charge modes are coupled together. After the critical point, an obvious separation between spin and charge excitations happens. Δ_c grows rapidly (linearly) by further increasing U, whereas Δ_s is slowly suppressed (with $1/U$). Note that none of the three excitation gaps can close for any $U > U_c$, and the system enters into a Mott insulator phase, with every lattice site being populated at $U \to \infty$. Since the low-energy excitation now possesses only spin degrees of freedom, Δ_{ne} coincides with Δ_s in this regime, as clearly demonstrated by our numerical results. To rule out the size effect, we do a finite-size scaling of different gaps after Mott transition. As shown in the inset of Fig. 2(b), Δ_c and Δ_s (Δ_{ne}) both tend to finite values in the thermodynamic limit, which is crucial for the protection of nontrivial topological properties.

The Mott transition at $U = U_c$ is of first order, with gap closings between ground and first excited states. Lattice translation symmetry forces $E_n(\varphi) = E_n(\varphi + \pi/3)$ at $\rho = 1$; therefore, there are six gap closings at $\varphi_p = p\pi/3$ ($0 \leqslant p \leqslant 5$ is an integer) in the whole evolution period of $\varphi \in [0, 2\pi]$. Across the Mott transition, the spin Chern number changes

six from $\mathcal{C}_s = 2$ to $\mathcal{C}_s = -4$, consistent with the simultaneous gap closing at six φ's.

The Mott transition is accompanied with SCS. After the transition, the Hamiltonian can be represented by two distinct sectors $H = H_c + H_s$. While the charge sector H_c is fully gapped out due to the strong interaction, the low-energy physics is governed by an effective spin sector H_s. A second-order perturbation theory at large U leads to an antiferromagnetic spin superexchange Hamiltonian (Appendix A 1)

$$H_s = \sum_j J\left[1 + \frac{(\mu_{j+1} - \mu_j)^2}{U^2}\right]\mathbf{S}_j \cdot \mathbf{S}_{j+1}, \qquad (3)$$

with periodically modulated exchange couplings. Here $\mathbf{S}_j = c_j^\dagger \boldsymbol{\sigma} c_j/2$ is the local spin operator at jth site. $J = 4t^2/U$ is the key energy scale of Mott physics and Δ_{ne} (Δ_s) decreases by $1/U$ to the leading order, which agrees with the DMRG results. From the standard bosonization theory [35], $m = -1/3$ is a quantized magnetization plateau that is topologically protected [13]. All the nontrivial properties can be understood from the above low-energy theory (Appendix A 2).

IV. BULK-EDGE CORRESPONDENCE

The appearance of edge states is usually considered as a hallmark of topological properties. We note that here the appearance of edge states in the superlattice system is attributed to the 2D topology, which is different from the typical 1D symmetry-protected topological phase (e.g., spin-1 Haldane phase [36,37]). Instead of ground-state degeneracy, gapless edge excitations emerge with the evolution of the superlattice phase φ. The topological properties are protected by charge and spin-S_z conservation symmetries. As SCS has severely changed the nature of low-energy excitations, bulk-edge correspondence of a topological Mott state is different. To this end, we study the low-energy spectrum under different boundary conditions and demonstrate the consequence of SCS. The charge distribution of a neutral excitation is $n_j^{ne} = n_j[\Psi_1(N_\uparrow, N_\downarrow)] - n_j[\Psi_0(N_\uparrow, N_\downarrow)]$. Here $[\Psi]$ represents taking the expectation value on state Ψ and $n_j = n_{j\uparrow} + n_{j\downarrow}$. Similarly, the spin distribution of a neutral excitation is $S_j^{ne} = S_j^z[\Psi_1(N_\uparrow, N_\downarrow)] - S_j^z[\Psi_0(N_\uparrow, N_\downarrow)]$ with $S_j^z = (n_{j\uparrow} - n_{j\downarrow})/2$. For each end, the accumulated charge (spin) is $n_l^{ne}(S_l^{ne}) = \sum_{j<L/2} n_j^{ne}(S_j^{ne})$ and $n_r^{ne}(S_r^{ne}) = \sum_{j>L/2} n_j^{ne}(S_j^{ne})$, respectively.

Our results are summarized in Fig. 3. Before SCS, the low-energy spectrum is fully gapped [Fig. 3(a)], while, under OBC, the ground state and first excited state cross at $\varphi = -\pi/3, 2\pi/3$ as shown in Fig. 3(c). Such boundary dependence indicates that, near these band crossings, the neutral excitations are gapless and localized at the ends. The crossings are reminiscent of the single-particle level crossings in Fig. 1(c). Due to the superlattice modulation, the charge and/or spin densities for both ground state and first excited state exhibit periodic oscillations. They share nearly the same distributions in the bulk, while being very different at two ends (Appendix A 4). Figure 3(e) plots the spatial distributions of spin and charge for one of the gapless neutral excitations. It is clear that the excitation carries both spin and charge degree of freedom at the two ends. Our numeric shows $n_l^{ne} = 1$,
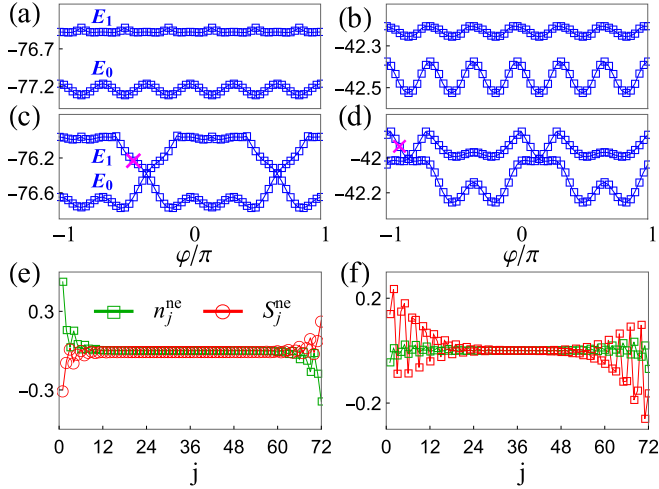
FIG. 3. Evolution of low-energy spectrum with φ under (a) PBC and (c) OBC for $U = 1$ and (b) PBC and (d) OBC for $U = 3.5$. Panels (e) and (f) represent the spatial distributions of charge n_j^{ne} (blue square) and spin S_j^{ne} (red circle) for the chosen neutral excitation modes [shown by "cross" in (c) and (d)], respectively. $\rho = 1$, $m = -1/3$, $\mu = 1.2$, $U = 3.5$, and $L = 72$.

FIG. 4. (a) Magnon spectrum $\Delta E_s(24, 48)$ and $\Delta E_s(25, 47)$ under PBC (blue square) and OBC (magenta circle) at filling $\rho = 1$. (b) Charge spectrum $\Delta E_c(24, 48)$ and $\Delta E_c(23, 47)$ under PBC (blue square) and OBC (magenta circle) for magnetization $m = -1/3$. (c) Spatial distributions of the two in-gap magnon modes [labeled by "cross" in (a)]. (d) Spatial distributions of the charge excitation at $\varphi = 0$. The double-headed arrows denote the spin and charge gaps. $\mu = 1.2$, $U = 3.5$, and $L = 72$.

$S_l^{ne} = -1/2$ for the left end and vice versa for the right end, which is in agreement with the bulk spin Chern number $\mathcal{C}_s = 2$ and validates the single-particle nature of these low-energy modes.

After SCS, the low-energy spectrum is fully gapped under PBC [Fig. 3(b)] and gapless end modes still emerge as shown in Fig. 3(d). Note that the appearance of these modes is at different φ's ($\varphi = -5\pi/6, \pi/6$), which can be understood from the adiabatic continuity (Appendix A 2) of the effective spin Hamiltonian (3). We have $n_{l,r}^{ne} = 0$, $S_{l,r}^{ne} = \pm 1$ for left and right ends [Fig. 3(f)]. These two pairs of spin-1 edge modes are consistent with bulk spin Chern number $\mathcal{C}_s = -4$.

Further, to describe the quantum correlations between two subsystems by a real-space partition, we calculate the entanglement spectrum. Our DMRG simulations show that the entanglement spectra for different phases exhibit similar band crossings with their low-energy spectra (Appendix A 3). With the increase of interaction strength, the entanglement entropy undergoes a sharp change and reaches its peak at the Mott transition point. Both the entanglement spectrum and entanglement entropy can be used as indicators of the Mott transition.

V. TOPOLOGICAL MAGNON EXCITATION

Starting from the many-body ground state $\Psi_0(N_\uparrow, N_\downarrow)$, we consider another two types of quasiparticle excitations. One is the magnon excitation purely in the spin sector with fixed total density. The quasiparticle spectrum is determined by the additional energy required to flip one spin-up to spin-down: $\Delta E_s(N_\uparrow, N_\downarrow) = E_0(N_\uparrow - 1, N_\downarrow + 1) - E_0(N_\uparrow, N_\downarrow)$. The spatial spin distribution of the quasiparticle is $\Delta S_j = S_j^z[\Psi_0(N_\uparrow - 1, N_\downarrow + 1)] - S_j^z[\Psi_0(N_\uparrow, N_\downarrow)]$. The other one is purely in the charge sector with fixed spin polarization (magnetization). The quasiparticle spectrum is determined by the additional energy required to add two atoms (one spin-up,
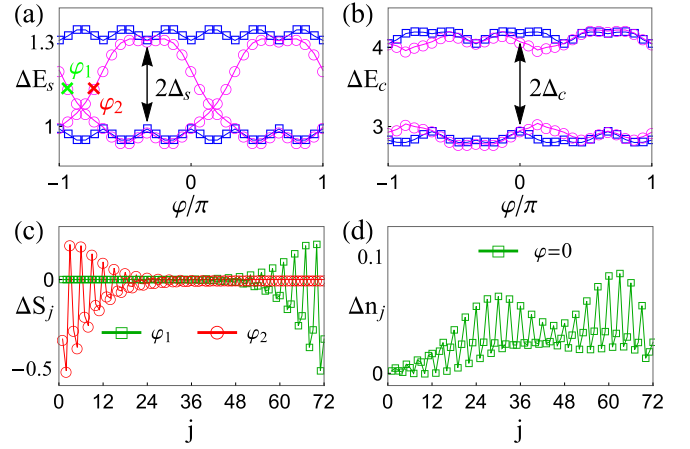
one spin-down) to the many-body system: $\Delta E_c(N_\uparrow, N_\downarrow) = E_0(N_\uparrow + 1, N_\downarrow + 1) - E_0(N_\uparrow, N_\downarrow)$. Its spatial charge distribution is $\Delta n_j = n_j[\Psi_0(N_\uparrow + 1, N_\downarrow + 1)] - n_j[\Psi_0(N_\uparrow, N_\downarrow)]$. These two types of quasiparticle excitations provide another perspective of the topological Mott physics.

In Figs. 4(a) and 4(b), we show their quasiparticle spectra after Mott transition. Under PBC, both spectra are split into two branches, separated by a finite magnon gap ($\sim 2\Delta_s$) and charge gap ($\sim 2\Delta_c$), respectively, while, under OBC, some in-gap magnon modes appear and cross at $\varphi = -5\pi/6$ and $\pi/6$ [Fig. 4(a)], similar to the low-energy excitations in Fig. 3(d). The distributions of the magnon excitations in two typical phases $\varphi = -14\pi/15$, $\varphi = -11\pi/15$ are shown in Fig. 4(c), which are well localized at the two ends. With the evolution of phase φ, these in-gap modes may touch the (top or bottom) bulk quasiparticle bands. Note that once such a band touching happens, the magnon modes would merge into the bulk and reappear on the other end. This is similar to the band touching between edge state and bulk bands [38] in the quantum Hall system. Furthermore, the magnon excitation, which is protected by a finite spin gap, is stable against disorder (Appendix A 5). The above nontrivial magnon excitations are closely related to the quantized magnetization plateau [13] of our effective model (3). As a comparison, the quasiparticle spectrum in the charge sector stays fully gapped under OBC as shown in Fig. 4(b). For any φ, the charge excitations distribute on the whole lattice [Fig. 4(d)], revealing the triviality in the charge sector.

VI. DISCUSSION AND SUMMARY

Our mechanism of inducing topological Mott insulator states based on SCS is quite general. The topological Mott physics here can be extended to (i) other period q (including the incommensurate case, i.e., the famous Aubry-André

model [39]), (ii) other fillings or magnetizations, and (iii) off-diagonal counterparts of model (1), i.e., triple-well lattices with periodic modulations on tunneling t, instead of on-site energy μ_j. The emergence of topological Mott insulator states with various spin Chern numbers and spinful edge modes is expected from our low-energy theory.

The proposed topological Mott insulator state and associated low-energy excitations can be experimentally probed in ultracold atomic gases. In addition to the proposed scheme using two sets of optical lattices, the 1D fermionic superlattice can also be generated using the recently developed digital micromirror device [40,41]. For fermionic ^{6}Li atoms [42,43], the wavelength of the laser beam is chosen as $\lambda = 1064$ nm, with the recoil energy $E_r \approx 2\pi\hbar \times 29.4$ kHz. At $V_0/E_r = 5$, $t \approx 2\pi\hbar \times 1.9$ kHz. The neutral and spin gaps of the topological Mott insulator state are then $\Delta_{ne} \approx 0.2t = 2\pi\hbar \times 390$ Hz, which is large enough (compared to temperature) to protect the topological properties [43]. These excitation gaps may be measured using radio-frequency spectroscopy [44–46]. The edge magnon excitations in the spin sector can be generated using a two-photon Raman process and their spin distributions at each site can be measured by detecting atomic spin distributions of different many-body ground states using spin-resolved quantum gas microscope [47–52] in optical lattices.

In summary, we have studied topological Mott transitions accompanied by SCS in a simple 1D optical superlattice, with low-energy excitations changing from single-particle spin-1/2 modes to bosonic spin-1 collective modes at the boundary. A topological Mott insulator state, characterized by spin Chern number and gapless magnon excitations, is identified. Our work may pave the way for the experimental observation of topological Mott insulator states in ultracold atomic gases.

APPENDIX

In this Appendix, we provide details on the derivation of the effective spin superexchange model, its topological properties which govern the low-energy physics, entanglement spectrum, the spatial charge and/or spin-density distributions of the many-body ground state, and the stability of the topological Mott phase against disorder.

1. Derivation of the effective spin superexchange model

We give a simple derivation of the effective spin superexchange model [Eq. (3) in the main text] using the second-order perturbation theory. To this end, we split the Hamiltonian [Eq. (1)] into two parts: $H = U n_{j\uparrow} n_{j\downarrow} + H_{\text{pert}}$, with $H_{\text{pert}} = \sum_{j,\sigma} [-t(c_{j\sigma}^\dagger c_{j+1\sigma} + \text{H.c.}) + \mu_j n_{j\sigma}]$ as the perturbation term. For the half-filling case $\rho = 1$ and $U \gg t$, the local Hilbert space on sites j and $j+1$ is spanned by the following four basis: $|\uparrow_j, \uparrow_{j+1}\rangle$, $|\uparrow_j, \downarrow_{j+1}\rangle$, $|\downarrow_j, \uparrow_{j+1}\rangle$, and $|\downarrow_j, \downarrow_{j+1}\rangle$. The effective Hamiltonian can be represented in this basis as $H_s = \sum_j H_{j,j+1}$, with

$$H_{j,j+1} = \begin{pmatrix} 0 & 0 & 0 & 0 \\ 0 & -\frac{t^2}{U+\mu_{j+1}-\mu_j} - \frac{t^2}{U+\mu_j-\mu_{j+1}} & \frac{t^2}{U+\mu_{j+1}-\mu_j} + \frac{t^2}{U+\mu_j-\mu_{j+1}} & 0 \\ 0 & \frac{t^2}{U+\mu_{j+1}-\mu_j} + \frac{t^2}{U+\mu_j-\mu_{j+1}} & -\frac{t^2}{U+\mu_{j+1}-\mu_j} - \frac{t^2}{U+\mu_j-\mu_{j+1}} & 0 \\ 0 & 0 & 0 & 0 \end{pmatrix}. \quad \text{(A1)}$$

Using spin-1/2 operator $\mathbf{S} = (S_x, S_y, S_z)$, the above Hamiltonian can be further represented as

$$H_s = \sum_j \frac{4t^2 U}{U^2 - (\mu_{j+1} - \mu_j)^2}[\mathbf{S}_j \cdot \mathbf{S}_{j+1} - 1/4]. \quad \text{(A2)}$$

By setting $J = \frac{4t^2}{U}$ and Taylor expanding the exchange coefficient by $1/U$ to the second order, we can get the effective spin superexchange model Eq. (3) after neglecting the constant term.

2. Adiabatic continuity and topological properties

Now we demonstrate the topological properties of the spin superexchange model, which dictates the low-energy physics of the system. To be more intuitive and clear, we introduce an anisotropy parameter g in $S_j^z S_{j+1}^z$ term:

$$H_s(g) = \sum_j J_j (S_j^x S_{j+1}^x + S_j^y S_{j+1}^y + g S_j^z S_{j+1}^z), \quad \text{(A3)}$$

with $J_j = J[1 + \frac{(\mu_{j+1}-\mu_j)^2}{U^2}]$. When $g = 1$, the above model recovers our low-energy Hamiltonian Eq. (3). The case $g = 0$ corresponds to an exactly solvable spin-XX chain by Jordan-Wigner transformation. We first show the nontrivial topology of $g = 0$ case and then demonstrate the adiabatic continuity in the whole region $g \geqslant 0$.

For $g = 0$, the Jordan-Wigner transformation (denoted $S_k^\pm = S_k^x \pm i S_k^y$)

$$d_j^\dagger = e^{i\pi \sum_{k=1}^{j-1} S_k^+ S_k^-} S_j^+, \quad d_j = e^{-i\pi \sum_{k=1}^{j-1} S_k^+ S_k^-} S_j^- \quad \text{(A4)}$$

takes the model (A3) to a spinless fermion model: $H_{J-W} = \sum_j J[1 + \frac{(\mu_{j+1}-\mu_j)^2}{U^2}](d_j^\dagger d_{j+1} + d_{j+1}^\dagger d_j)$. The band structure of
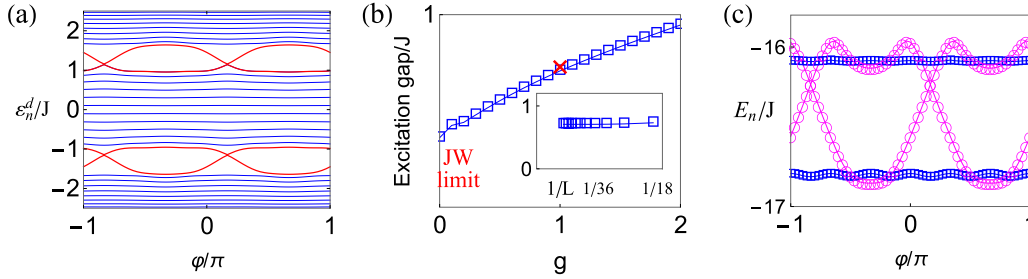
FIG. 5. (a) Single-particle band of Jordan-Wigner fermions, $g = 0$. (b) Excitation gap with respect to anisotropy parameter g. The inset shows its finite-size scaling at $g = 1$ and $\varphi = 0$. (c) The lowest two eigenenergies of model (A3) under OBC (magenta circle) and PBC (blue square) with the evolution of φ. $\mu^2/U^2 = 0.2$ for all figures.

H_{J-W} is shown in Fig. 5(a). Due to the periodically modulated hoppings of Jordan-Wigner fermions, the single-particle spectrum ε_n^d consists of three (bulk) topological bands and gapless end modes inside the band gap with the evolution of phase φ under OBC. Notice that, different from the original single-particle band in Fig. 1, these end modes now cross at $\varphi = -5\pi/6$ and $\varphi = \pi/6$ [consistent with the DMRG results in Figs. 3(b) and 4(a) in the main text] and correspond to (spinful) low-energy collective modes.

To demonstrate the adiabatic continuity in the whole region $g \geqslant 0$, we plot the excitation gap (energy difference between the ground state and first excited state) of model (A3) with respect to g in Fig. 5(b). With increasing g from Jordan-Wigner limit $g = 0$, the excitation gap increases. From the scaling behavior of the gap [inset of Fig. 5(b)], we can see it tends to a finite value in the thermodynamical limit at $g = 1$. The above adiabatic continuity reveals that our effective spin superexchange model H_s has the same topological properties as those of Jordan-Wigner fermions.

Furthermore, we show the low-energy spectrum of the spin superexchange model Eq. (3) in Fig. 5(c). Although there always exists an excitation gap at any φ under PBC, the ground state and first excited state touch at $\varphi = -5\pi/6$ and $\varphi = \pi/6$ under OBC [consistent with the DMRG results in Figs. 3(b) and 4(a) in the main text]. As these crossings depend on the boundary condition, the excitations around these touching points are well-localized end modes (not shown). For example, at $\varphi = -9\pi/10$, our numeric gives accumulated spin distribution $\Delta S_z = 0.9996$ on the left end and $\Delta S_z = -0.9996$ on the right end. The integer spinful end modes

are consistent with those neutral excitations in the main text [Fig. 3(f) in the main text].

3. Entanglement spectrum

Entanglement spectrum (ES), which describes the quantum correlations between two subsystems (A and B), provides another perspective to investigate the topological properties of quantum many-body systems [53]. Through a real-space partition, the ES can be directly obtained from the eigenvalues of the reduced density matrix of the subsystem. Formally, the total density matrix associated with state $|\Psi\rangle$ is $\rho = |\Psi\rangle\langle\Psi|$. By taking the trace over the degrees of freedom in one of the subsystems (for example B), we can get the reduced density matrix of subsystem A:

$$\rho_A = \mathrm{tr}_B(\rho). \tag{A5}$$

An eigenvalue decomposition of ρ_A yields

$$\rho_A = \sum_n \omega_n |\Phi_n^A\rangle\langle\Phi_n^A|. \tag{A6}$$

The eigenvalue spectrum ω_n, which gives the weight in the Schmidt decomposition, forms the ES. In DMRG algorithm, the ES can be directly obtained from the superblock ground state $|\Psi\rangle = \sum_{m,n} F^{m,n} |\Psi_m^A\rangle |\Psi_n^B\rangle$, where $|\Psi_m^A\rangle$ and $|\Psi_m^B\rangle$ are the orthonormal basis in the two (block) Hilbert spaces and $F^{m,n}$ is a rectangular matrix. By singular-value decomposition $F = UDV'$, we have

$$|\Psi\rangle = \sum_n \lambda_n |\Phi_n^A\rangle |\Phi_n^B\rangle. \tag{A7}$$

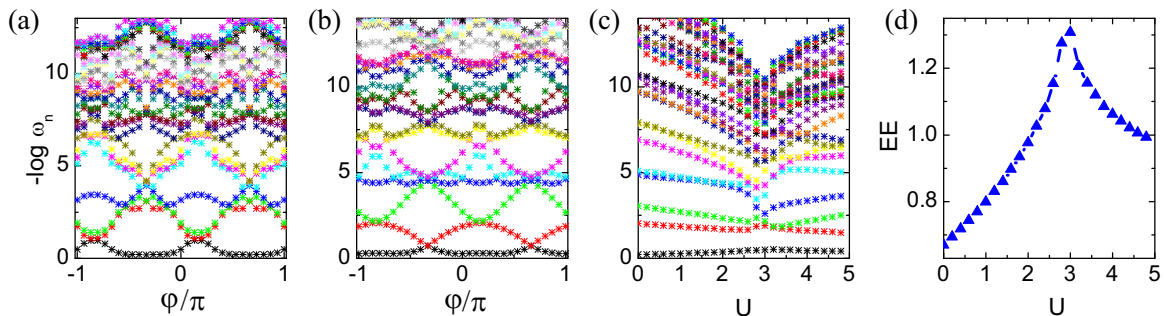FIG. 6. Entanglement spectrum (ES) for model (1) in the main text. (a) ES with respect to φ before spin-charge separation, $U = 1$. (b) ES with respect to φ after spin-charge separation, $U = 3.5$. (c) ES as a function of interaction strength U, $\varphi = 0$. (d) Entanglement entropy (EE) as a function of U. In the calculation of the ES, OBC is applied. Other parameters are $\mu = 1.2$ and $L = 72$.
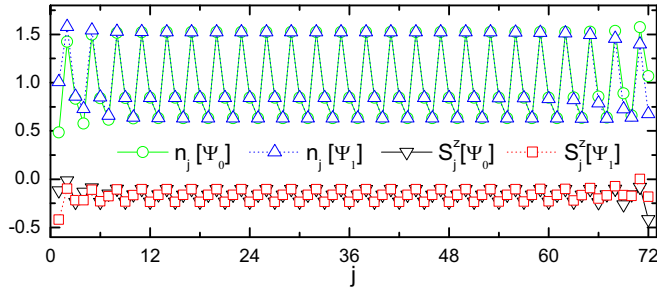
FIG. 7. Charge density n_j and spin density S_j^z for the many-body ground state Ψ_0 and first excited state Ψ_1. Their difference gives the spatial charge and/or spin distributions of the low-energy (neutral) excitation [see Fig. 3(e) in the main text], which are localized at the two ends. The parameters are the same as Fig. 3(e).

Obviously, the ES is given by $\omega_n = |\lambda_n|^2$. Based on the ES, the entanglement entropy (EE) is defined as

$$\mathrm{EE} = -\sum_n \omega_n \log \omega_n. \qquad (A8)$$

The main results of our DMRG simulations are summarized in Fig. 6. For the two topological phases (before and after spin-charge separation) of model (1), their ES with respect to the superlattice phase φ [Figs. 6(a) and 6(b)] exhibits similar band crossings as the low-energy spectrum [Figs. 3(c) and 3(d) in the main text], revealing the gapless nature of the edge modes. Either ES or EE can be further used as an indicator of the topological phase transition as shown in Figs. 6(c) and 6(d). At the transition point $U = U_c$, the ES as well as EE undergoes a sharp change.

4. Spatial charge and spin-density distributions

In this section, we illustrate the spatial charge and/or spin-density distributions of the ground state Ψ_0 and first excited state Ψ_1 from DMRG simulations. Due to the spatial modulations of the superlattice, both charge and spin densities exhibit periodic oscillations (with period q of the superlattice). Let us take the topological phase before spin-charge separation as an example (the conclusions are the same for the topological Mott phase after spin-charge separation), as depicted in Fig. 7.
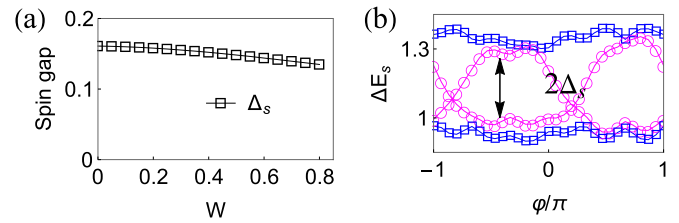

FIG. 8. Topological Mott phase with disorder. (a) Spin-gap Δ_s with respect to the disorder strength W under PBC. Here for each disorder strength, Δ_s is averaged over 50 different realizations of random disorder. (b) Magnon spectrum $\Delta E_s(24, 48)$ and $\Delta E_s(25, 47)$ under PBC (blue square) and OBC (magenta circle) with respect to the superlattice phase φ. $W = 0.5$. Other parameters are the same as Fig. 4 in the main text, i.e., $\mu = 1.2$, $U = 3.5$, and $L = 72$.

It is clear that while the two many-body states (Ψ_0 and Ψ_1) share nearly the same charge and/or spin distributions in the bulk, they do not at the two ends. Their differences give the corresponding charge and/or spin distributions of the neutral excitation, i.e., $n_j^{ne} = n_j[\Psi_1] - n_j[\Psi_0]$ and $S_j^{ne} = S_j^z[\Psi_1] - S_j^z[\Psi_0]$. Hence the neutral excitations are mainly localized at the two ends, as shown in Fig. 3(e) in the main text.

5. Stability against disorder

The topological Mott phase, which is protected by a finite excitation gap (spin gap), is stable against disorder. We introduce disorder through the random on-site energy with a uniform distribution within $[-W, W]$, where W is the disorder strength. Our DMRG results are summarized in Fig. 8.

First, we show the dependence of the spin gap Δ_s with respect to the disorder strength W in Fig. 8(a). With increasing W, the spin gap slightly decreases. The numeric shows Δ_s changes by 16% up to $W = 0.8$. Next, we demonstrate the stability of edge modes against disorder. We take the magnon excitation as an example. Figure 8(b) depicts the magnon spectra under OBC and PBC for a medium disorder strength $W = 0.5$. It is clear that, inside the bulk magnon gap, there still exist in-gap magnon excitations, which are localized at the two ends. All these results indicate that the topological Mott phase survives to a large disorder strength.

[1] M. Z. Hasan and C. L. Kane, *Colloquium*: Topological insulators, Rev. Mod. Phys. **82**, 3045 (2010).

[2] X.-L. Qi and S. C. Zhang, Topological insulators and superconductors, Rev. Mod. Phys. **83**, 1057 (2011).

[3] D. C. Tsui, H. L. Stormer, and A. C. Gossard, Two-Dimensional Magnetotransport in the Extreme Quantum Limit, Phys. Rev. Lett. **48**, 1559 (1982).

[4] R. B. Laughlin, Anomalous Quantum Hall Effect: An Incompressible Quantum Fluid with Fractionally Charged Excitations, Phys. Rev. Lett. **50**, 1395 (1983).

[5] S. Raghu, X.-L. Qi, C. Honerkamp, and S.-C. Zhang, Topological Mott Insulators, Phys. Rev. Lett. **100**, 156401 (2008).

[6] D. Pesin, L. Balents, Mott physics and band topology in materials with strong spin-orbit interaction, Nat. Phys. **6**, 376 (2010).

[7] T. Yoshida, R. Peters, S. Fujimoto, and N. Kawakami, Characterization of a Topological Mott Insulator in One Dimension, Phys. Rev. Lett. **112**, 196404 (2014).

[8] L.-J. Lang, X. M. Cai, and S. Chen, Edge States and Topological Phases in One-Dimensional Optical Superlattices, Phys. Rev. Lett. **108**, 220401 (2012).

[9] Y. E. Kraus, Y. Lahini, Z. Ringel, M. Verbin, and O. Zilberberg, Topological States and Adiabatic Pumping in Quasicrystals, Phys. Rev. Lett. **109**, 106402 (2012).

[10] S.-L. Zhu, Z.-D. Wang, Y.-H. Chan, and L.-M. Duan, Topological Bose-Mott Insulators in a One-Dimensional Optical Superlattice, Phys. Rev. Lett. **110**, 075303 (2013).

[11] Z. H. Xu, L. H. Li, and S. Chen, Fractional Topological States of Dipolar Fermions in One-Dimensional Optical Superlattices, Phys. Rev. Lett. **110**, 215301 (2013).

[12] Z. H. Xu and S. Chen, Topological Mott insulators of ultracold atomic mixtures induced by interactions in one-dimensional optical superlattices, Phys. Rev. B **88**, 045110 (2013).

[13] H. P. Hu, C. Cheng, Z. H. Xu, H.-G. Luo, and S. Chen, Topological nature of magnetization plateaus in periodically modulated quantum spin chains, Phys. Rev. B **90**, 035150 (2014).

[14] H. P. Hu, H. M. Guo, and S. Chen, Fractional topological states in quantum spin chains with periodical modulation, Phys. Rev. B **93**, 155133 (2016).

[15] Y. Kuno, K. Shimizu, and I. Ichinose, Various topological Mott insulators and topological bulk charge pumping in strongly-interacting boson system in one-dimensional superlattice, New J. Phys. **19**, 123025 (2017).

[16] L. Stenzel, A. L. C. Hayward, C. Hubig, U. Schollwöck, and F. Heidrich-Meisner, Quantum phases and topological properties of interacting fermions in one-dimensional superlattices, Phys. Rev. A **99**, 053614 (2019).

[17] D. R. Hofstadter, Energy levels and wave functions of Bloch electrons in rational and irrational magnetic fields, Phys. Rev. B **14**, 2239 (1976).

[18] P. G. Harper, The general motion of conduction electrons in a uniform magnetic field, with application to the diamagnetism of metals, Proc. Phys. Soc. A **68**, 874 (1955).

[19] G. Roati, C. D'Errico, L. Fallani, M. Fattori, C. Fort, M. Zaccanti, G. Modugno, M. Modugno, and M. Inguscio, Anderson localization of a non-interacting Bose-Einstein condensate, Nature (London) **453**, 895 (2008).

[20] L. Fallani, J. E. Lye, V. Guarrera, C. Fort, and M. Inguscio, Ultracold Atoms in a Disordered Crystal of Light: Towards a Bose Glass, Phys. Rev. Lett. **98**, 130404 (2007).

[21] M. Schreiber *et al.*, Observation of many-body localization of interacting fermions in a quasirandom optical lattice, Science **349**, 842 (2015).

[22] V. Guarrera, L. Fallani, J. E. Lye, C. Fort, and M. Inguscio, Inhomogeneous broadening of a Mott insulator spectrum, New J. Phys. **9**, 107 (2007).

[23] G. Roux, T. Barthel, I. P. McCulloch, C. Kollath, U. Schollwöck, and T. Giamarchi, Quasiperiodic Bose-Hubbard model and localization in one-dimensional cold atomic gases, Phys. Rev. A **78**, 023628 (2008).

[24] B. Damski, J. Zakrzewski, L. Santos, P. Zoller, and M. Lewenstein, Atomic Bose and Anderson Glasses in Optical Lattices, Phys. Rev. Lett. **91**, 080403 (2003).

[25] T. Roscilde, Bosons in one-dimensional incommensurate superlattices, Phys. Rev. A **77**, 063605 (2008).

[26] D. J. Thouless, Quantization of particle transport, Phys. Rev. B **27**, 6083 (1983).

[27] M. Olshanii, Atomic Scattering in the Presence of An External Confinement and a Gas of Impenetrable Bosons, Phys. Rev. Lett. **81**, 938 (1998).

[28] D. Xiao, M.-C. Chang, and Q. Niu, Berry phase effects on electronic properties, Rev. Mod. Phys. **82**, 1959 (2010).

[29] Q. Niu, D. J. Thouless, and Y.-S. Wu, Quantized Hall conductance as a topological invariant, Phys. Rev. B **31**, 3372 (1985).

[30] Y. Qian, M. Gong, and C. Zhang, Quantum transport of bosonic cold atoms in double well optical lattices, Phys. Rev. A **84**, 013608 (2011).

[31] L. Wang, M. Troyer, and X. Dai, Topological Charge Pumping in a One-Dimensional Optical Lattice, Phys. Rev. Lett. **111**, 026802 (2013).

[32] S. Nakajima, T. Tomita, S. Taie, T. Ichinose, H. Ozawa, L. Wang, M. Troyer, and Y. Takahashi, Topological Thouless pumping of ultracold fermions, Nat. Phys. **12**, 296 (2016).

[33] D. N. Sheng, L. Balents, and Z. Q. Wang, Phase Diagram for Quantum Hall Bilayers at $\nu = 1$, Phys. Rev. Lett. **91**, 116802 (2003).

[34] D. N. Sheng, Z. Y. Weng, L. Sheng, and F. D. M. Haldane, Quantum Spin-Hall Effect and Topologically Invariant Chern Numbers, Phys. Rev. Lett. **97**, 036808 (2006).

[35] M. Oshikawa, M. Yamanaka, and I. Affleck, Magnetization Plateaus in Spin Chains: "Haldane Gap" for Half-Integer Spins, Phys. Rev. Lett. **78**, 1984 (1997).

[36] F. D. M. Haldane, Continuum dynamics of the 1-D Heisenberg antiferromagnet: Identification with the $O(3)$ nonlinear sigma model, Phys. Lett. A **93**, 464 (1983).

[37] I. Affleck, T. Kennedy, E. H. Lieb, and H. Tasaki, Valence bond ground states in isotropic quantum antiferromagnets, Commun. Math. Phys. **115**, 477 (1988).

[38] Y. Hatsugai, Chern Number and Edge States in the Integer Quantum Hall Effect, Phys. Rev. Lett. **71**, 3697 (1993).

[39] S. Aubry and G. André, Analyticity breaking and Anderson localization in incommensurate lattices, Ann. Isr. Phys. Soc. **3**, 133 (1980).

[40] M. E. Tai, A. Lukin, M. Rispoli, R. Schittko, T. Menke, D. Borgnia, P. M. Preiss, F. Grusdt, A. M. Kaufman, and M. Greiner, Microscopy of the interacting Harper–Hofstadter model in the two-body limit, Nature (London) **546**, 519 (2017).

[41] P. Zupancic, P. M. Preiss, R. Ma, A. Lukin, M. E. Tai, M. Rispoli, R. Islam, and M. Greiner, Ultra-precise holographic beam shaping for microscopic quantum control, Opt. Express **24**, 13881 (2016).

[42] R. A. Hart, P. M. Duarte, T.-L. Yang, X. Liu, T. Paiva, E. Khatami, R. T. Scalettar, N. Trivedi, D. A. Huse, and R. G. Hulet, Observation of antiferromagnetic correlations in the Hubbard model with ultracold atoms, Nature (London) **519**, 211 (2015).

[43] A. Mazurenko, C. S. Chiu, G. Ji, M. F. Parsons, M. Kanász-Nagy, R. Schmidt, F. Grusdt, E. Demler, D. Greif, and M. Greiner, A cold-atom Fermi-Hubbard antiferromagnet, Nature (London) **545**, 462 (2017).

[44] C. Chin, M. Bartenstein, A. Altmeyer, S. Riedl, S. Jochim, J. Hecker Denschlag, and R. Grimm, Observation of the pairing gap in a strongly interacting Fermi gas, Science **305**, 1128 (2004).

[45] G. K. Campbell, J. Mun, M. Boyd, P. Medley, A. E. Leanhardt, L. Marcassa, D. E. Pritchard, and W. Ketterle, Imaging the Mott insulator shells by using atomic clock shifts, Science **313**, 649 (2006).

[46] S. Kato, K. Inaba, S. Sugawa, K. Shibata, R. Yamamoto, M. Yamashita, and Y. Takahashi, Laser spectroscopic probing of coexisting superfluid and insulating states of an atomic Bose–Hubbard system, Nat. Commun. **7**, 11341 (2016).

[47] W. S. Bakr, J. I. Gillen, A. Peng, S. Fölling, and M. Greiner, A quantum gas microscope for detecting single atoms in a Hubbard-regime optical lattice, Nature (London) **462**, 74 (2009).

[48] J. F. Sherson, C. Weitenberg, M. Endres, M. Cheneau, I. Bloch, and S. Kuhr, Single-atom-resolved fluorescence imaging of an atomic Mott insulator, Nature (London) **467**, 68 (2010).

[49] L. W. Cheuk, M. A. Nichols, M. Okan, T. Gersdorf, V. V. Ramasesh, W. S. Bakr, T. Lompe, and M. W. Zwierlein, Quantum-Gas Microscope for Fermionic Atoms, Phys. Rev. Lett. **114**, 193001 (2015).

[50] E. Haller, J. Hudson, A. Kelly, D. A. Cotta, B. Peaudecerf, G. D. Bruce, and S. Kuhr, Single-atom imaging of fermions in a quantum-gas microscope, Nat. Phys. **11**, 738 (2015).

[51] M. F. Parsons, F. Huber, A. Mazurenko, C. S. Chiu, W. Setiawan, K. Wooley-Brown, S. Blatt, and M. Greiner, Site-resolved Imaging of Fermionic ^{6}Li in an Optical Lattice, Phys. Rev. Lett. **114**, 213002 (2015).

[52] M. F. Parsons, A. Mazurenko, C. S. Chiu, G. Ji, D. Greif, and M. Greiner, Site-resolved measurement of the spin-correlation function in the Fermi-Hubbard model, Science **353**, 1253 (2016).

[53] H. Li and F. D. M. Haldane, Entanglement Spectrum as a Generalization of Entanglement Entropy: Identification of Topological Order in Non-Abelian Fractional Quantum Hall Effect States, Phys. Rev. Lett. **101**, 010504 (2008).